

# Accepted Manuscript

Revealing the microstructural stability of a three-phase soft solid (ice cream) by 4D synchrotron X-ray tomography

Enyu Guo, Daniil Kazantsev, Jingyi Mo, Julian Bent, Gerard Van Dalen, Peter Schuetz, Peter Rockett, David StJohn, Peter D. Lee



PII: S0260-8774(18)30230-9

DOI: [10.1016/j.jfoodeng.2018.05.027](https://doi.org/10.1016/j.jfoodeng.2018.05.027)

Reference: JFOE 9271

To appear in: *Journal of Food Engineering*

Received Date: 29 January 2018

Revised Date: 8 May 2018

Accepted Date: 24 May 2018

Please cite this article as: Guo, E., Kazantsev, D., Mo, J., Bent, J., Van Dalen, G., Schuetz, P., Rockett, P., StJohn, D., Lee, P.D., Revealing the microstructural stability of a three-phase soft solid (ice cream) by 4D synchrotron X-ray tomography, *Journal of Food Engineering* (2018), doi: 10.1016/j.jfoodeng.2018.05.027.

This is a PDF file of an unedited manuscript that has been accepted for publication. As a service to our customers we are providing this early version of the manuscript. The manuscript will undergo copyediting, typesetting, and review of the resulting proof before it is published in its final form. Please note that during the production process errors may be discovered which could affect the content, and all legal disclaimers that apply to the journal pertain.

1 **Revealing the microstructural stability of a three-phase soft solid**  
2 **(ice cream) by 4D synchrotron X-ray tomography**

3  
4 Enyu Guo <sup>a,c,\*\*</sup>, Daniil Kazantsev <sup>c,d</sup>, Jingyi Mo <sup>b,c</sup>, Julian Bent <sup>e</sup>,  
5 Gerard Van Dalen <sup>e</sup>, Peter Schuetz <sup>e</sup>, Peter Rockett <sup>b</sup>, David StJohn <sup>f</sup>, Peter D Lee <sup>b,c,\*</sup>

6  
7 <sup>a</sup>Key Laboratory of Solidification Control and Digital Preparation  
8 Technology (Liaoning Province), School of Materials Science and Engineering,  
9 Dalian University of Technology, Dalian, 116024, China

10  
11 <sup>b</sup>Department of Mechanical Engineering, University College London, Torrington  
12 Place, London WC1E 7JE, UK

13  
14 <sup>c</sup>Research Complex at Harwell, RAL, Didcot, OX11 0FA, UK

15  
16 <sup>d</sup>The Manchester X-Ray Imaging Facility, School of Materials, The University of  
17 Manchester, Manchester, M13 9PL, UK

18  
19 <sup>e</sup>Unilever R&D, Colworth, MK44 1LQ, UK

20  
21 <sup>f</sup>School of Mechanical and Mining Engineering, The University of Queensland,  
22 St Lucia, Queensland, 4072, Australia

23  
24  
25  
26  
27 Submitted to

28  
29 **Journal of Food Engineering**

30  
31 In revised version  
32 May 2018

33  
34  
35  
36  
37  
38 <sup>\*,\*\*</sup>Corresponding authors:

39 <sup>\*</sup>Peter D Lee: [peter.lee@ucl.ac.uk](mailto:peter.lee@ucl.ac.uk); Tel: +44 (0)1235 567789

40 <sup>\*\*</sup>Enyu Guo: [eyguo@dlut.edu.cn](mailto:eyguo@dlut.edu.cn); Tel: +86 (0)411 84709500

43

44

**Abstract**

45 Understanding the microstructural stability of soft solids is key to optimizing  
46 formulations and processing parameters to improve the materials' properties. In this  
47 study, *in situ* synchrotron X-ray tomography is used to determine the temperature  
48 dependence of ice-cream's microstructural evolution, together with the underlying  
49 physical mechanisms that control microstructural stability. A new tomographic data  
50 processing method was developed, enabling the features to be segmented and  
51 quantified. The time-resolved results revealed that the melting-recrystallization  
52 mechanism is responsible for the evolution of ice crystal size and morphology during  
53 thermal cycling between -15 and -5 °C, while coalescence of air cells is the dominant  
54 coarsening mechanism controlling air bubble size and interconnectivity. This work  
55 also revealed other interesting phenomena, including the role of the unfrozen matrix  
56 in maintaining the ice cream's microstructural stability and the complex interactions  
57 between ice crystals and air structures, e.g. the melting and recrystallization of ice  
58 crystals significantly affect the air cell's morphology and the behavior of the unfrozen  
59 matrix. The results provide crucial information enhancing the understanding of  
60 microstructural evolution in multi-phase multi-state complex foodstuffs and other soft  
61 solids.

62

63 **Keywords:** Ice cream; Microstructure; Tomography; Ice crystals; Coarsening; Soft  
64 solid.

65

## 66 1. Introduction

67 Soft solids are important composites that are characterized by complex  
68 multi-phase structures and possess inherently complex non-Newtonian rheological  
69 properties under external stress [1-3]. Soft solids exist either in nature, e.g. muds, or  
70 in many artificially manufactured products such as emulsions, biopolymers, fresh  
71 concrete and domestic baking materials. Many soft solids, such as soft foams (e.g. ice  
72 cream) and aerated desserts, contain porous phases within a viscous matrix [4-6].

73 Structural stability is desired for many soft foams and microstructural instability  
74 greatly influences the materials' properties and their applications. Take ice cream for  
75 example. The microstructure of ice cream, including the size distribution and  
76 connectivity of each phase, plays a critical role in determining product quality (e.g.  
77 mouthfeel, taste, appearance, etc.) and the product's shelf-life [6-10]. For example,  
78 the microstructural change at different storage temperatures has been shown to alter  
79 ice cream's viscoelastic properties and hence the oral sensory perception of it [10].  
80 However, irreversible microstructural changes often occur in ice creams (over a range  
81 of different timescales), as well as in other similar foam structures that contain air,  
82 above a certain temperature ( $\sim -30$  °C for ice cream [4]) which may occur during  
83 shipping, storage at the grocery store and in domestic freezers (ca.  $-18$  °C), and on the  
84 consumer's table.

85 For ice cream, the structural instability is affected by many factors, including  
86 compositions [11, 12] and thermal variations [5, 13]. One of the well-recognized  
87 phenomena due to thermal instability is coarsening of microstructure [4, 5, 13-15].  
88 This was initially examined in light microscopy [14, 16-19] and cryo-scanning

89 electron microscopy [20, 21], and transmission electron microscopy [22], all of which  
90 provide only 2D information of the surface or of cuts through the ice cream sample.  
91 These phenomena were recently studied in 3D with X-ray tomography on *ex situ*  
92 coarsened samples [4, 5]. Using a synchrotron X-ray tomography technique, prior  
93 work by the same authors [5] revealed that after thermal cycling (or thermal ‘abuse’)  
94 between -15 and -5 °C for a number of cycles/days, both ice crystals and air cells  
95 grew in size creating ice dominated structures within a deteriorated ice cream  
96 microstructure. More specifically, the size of ice crystals was observed to  
97 continuously increase up to 14 cycles; however, the growth rate significantly  
98 decreased after 7 thermal cycles. The air cells also increased in size, and they  
99 continued to grow into interconnected irregular shapes with long continuous channels  
100 after 14 thermal cycles. However, for up to 7 thermal cycles the air cells seemed to  
101 remain more or less spherical.

102 From that *ex situ* study, it was observed that the ice crystals within the unfrozen  
103 matrix tended to align along the boundary between air cells and the matrix,  
104 minimizing surface energy. Those 3D experiments provided valuable insight into the  
105 structural changes of ice cream upon thermal cycling. However, the study was  
106 performed on *ex situ* thermally cycled samples and thus, the interactions between the  
107 microstructural features could not be elucidated. The detailed mechanisms that control  
108 the microstructural evolution, which are only available via *in situ* studies, still remain  
109 to be explored. Questions regarding the growth mechanisms and relative movement of  
110 the phases and their exact interactions during thermal cycling, need to be answered to

111 be able to improve the stability of the ice cream's structure [5, 14, 23]. For example,  
112 what are the dynamics of the changes for each phase and how do they impose on each  
113 other due to thermal variations, in order to maintain the integrity of ice cream's  
114 structure? What are the dominant coarsening mechanisms that control the ice cream's  
115 microstructural evolution?

116 This work non-destructively studies the thermal stability of the ice cream  
117 microstructure via 4D (3D plus time) synchrotron X-ray tomography to reveal the  
118 dynamics of the microstructural changes. This technique has become increasingly  
119 used in the study of opaque materials systems to study both coarsening [24] and  
120 rheology during deformation [25, 26]. X-ray tomographs were continuously acquired  
121 on a sample during a heating and cooling cycle at a well-controlled slow ramp rate of  
122 0.05 °C/min. To analyze the acquired data, an iterative tomographic data  
123 reconstruction and image processing method was developed. Through quantitative  
124 analysis, the physical mechanisms which dominate the degradation of ice cream's  
125 microstructure due to temperature variation, are examined and discussed in detail.

126

## 127 **2. Materials and methods**

### 128 **2.1 Sample and experimental methods**

129 Fresh ice cream containing 5% fat was manufactured by Unilever R&D (U. K). A  
130 500 ml block of fresh ice cream was initially thermally cycled between -15 and -5 °C  
131 for seven times (1 week) before it was used for the *in situ* synchrotron experiment.  
132 The seven cycles created a larger scale of microstructure, enabling easy identification  
133 of phases for quantification, and also represent a transition point between the

134 observations made in the first seven cycles where change was relatively rapid and the  
135 next seven cycles where the size of ice crystals became more stable as reported in the  
136 authors' prior *ex situ* studies [5]. Small ice cream samples, each contained in a 3 mm  
137 inner diameter kapton tube (67  $\mu\text{m}$  thick, American Durafilm Co. Inc, Holliston, U.S),  
138 were cut from the 500 ml block. Details of the sample preparation method are  
139 described in [5].

140 The *in situ* synchrotron experiment was conducted on the Diamond Manchester  
141 Beamline (I13-2) of the Diamond Light Source (DLS, U.K) using a pink beam. The  
142 set-up for running the beamline experiment, together with the cold stage used to  
143 provide the sample temperature, is described in [5, 27]. During the *in situ* thermal  
144 cycling experiment, the sample was loaded in the cold stage at  $-15\text{ }^{\circ}\text{C}$  and stabilized  
145 for 10 min. Then, the sample was heated to  $-5\text{ }^{\circ}\text{C}$  at a ramp rate of 0.05 K/min and  
146 held there for 10 min. After that, the sample was cooled back to  $-15\text{ }^{\circ}\text{C}$  at the same  
147 ramp rate as the heating stage. A schematic of the thermal cycle history is shown in  
148 the inset of Fig. 1. The tomographic scans were acquired using a  $2560 \times 2160$  pixel  
149 PCO Edge 5.5 CMOS camera that was optically coupled to a single crystal  $\text{CdWO}_4$   
150 scintillator during the thermal cycle. For each tomographic scan, 900 projections were  
151 recorded with an exposure time of 100 ms (90 s for each scan) and a pixel size of 0.8  
152  $\mu\text{m}$ . However, at the end of each tomographic scan, the sample stage was rotated back  
153 to the initial position for system re-initiation to start the next tomographic scan,  
154 adding an additional delay of  $\sim 51\text{ s}$ , for a cycle time of  $\sim 141\text{ s}$ . In total, 178  
155 tomographic scans were acquired during a thermal cycle.

## 156 2.2 Image reconstruction and three-phase segmentation approach

157 Initially, the acquired projection data were reconstructed using the conventional  
158 Filtered Back Projection (FBP) algorithm [28], producing extremely noisy  
159 reconstructions with low contrast and ring artifacts (see Fig. 2(a)). The poor quality of  
160 FBP images was due to angular under-sampling (only 900 projections for a  $2k \times 2k \times$   
161  $2k$  volume), short exposure time and low attenuation contrast between ice and water.  
162 In order to improve the image quality suitable for segmentation, a Model-Based  
163 Iterative Reconstruction (MBIR) approach was applied.

164 The MBIR algorithm is based on the Group-Huber data fidelity function to  
165 minimize ring artifacts and 3D total variation (TV) regularization penalty [29-31].  
166 The TV-related regularization sub-problem has been solved using the Split-Bregman  
167 method in order to enhance the weak contrast between ice crystals and unfrozen  
168 matrix (see Fig. 2(b)).

169 Although MBIR reconstruction substantially improves the contrast and also  
170 removes noise, the reconstructed images suffer from the visible intensity  
171 inhomogeneities within various ice-crystals (indicated by arrows in Fig. 2(b)). These  
172 artifacts can be a result of the combined effects of strong noise and beam hardening.  
173 The latter is possible due to abrupt changes in attenuation coefficients between  
174 unfrozen matrix (highly attenuated) and ice crystals (poorly attenuated), therefore  
175 introducing non-linearity in a beam. Intensity inhomogeneity within a single crystal  
176 restricts successful segmentation by histogram thresholding. One can use more  
177 sophisticated segmentation methods (e.g. 3D snake contours can successfully segment  
178 features with intensity inhomogeneity using supervised seeding). However, due to the



179 large data size, a computationally efficient approach is required.

180 Here an additional post-processing step was applied to equalize intensity within  
181 phases by means of gradient-constrained nonlinear isotropic diffusion [5, 32]. The  
182 mask to terminate the diffusion process across selected boundaries was acquired from  
183 the image in Fig. 2(b) by thresholding the magnitude of the gradient. Since the  
184 gradient magnitude between phases is large and the variations of intensity within  
185 regions are gradual, one can run the constrained diffusion until the regions become  
186 fully homogeneous. Therefore, 1000 diffusion iterations were run on a GPU to  
187 equalize intensities within enclosed regions of the image in Fig. 2(b). The result (Fig.  
188 2(c)) is sufficient to implement a simple histogram thresholding operation and  
189 generate images with homogeneous contrast within three phases (Fig. 2(d)).

190 Finally, the processed volume was cropped into a smaller volume for 3D analysis.  
191 3D rendering of the features, as well as quantification of size/volume, was performed  
192 using Avizo® (FEI, Thermo Fisher Scientific, U. S). The thickness of unfrozen matrix  
193 was measured using BoneJ in ImageJ [33].

194

### 195 **3. Results and Discussion**

#### 196 **3.1 General microstructural evolution during thermal cycling**

197 Fig. 3 and supplementary Fig. S1 show the 2D tomographic slices of ice cream's  
198 microstructural evolution during thermal cycling between -15 and -5 °C. A few salient  
199 observations can be made based on these images. First, ice crystals were continuously  
200 melting, decreasing in size, during the heating stage (Fig. 3(a-c)) and their

201 morphologies became more spherical at “high” temperature (e.g.  $-5\text{ }^{\circ}\text{C}$ , Fig. 3(c)). It  
202 appears that the most significant morphologic change took place in the temperature  
203 range  $-7.5$  to  $-5\text{ }^{\circ}\text{C}$ . During cooling, the relatively round ice crystals grow into a more  
204 irregular morphology again (Fig. 3(d-f)), as expected for ice which has a high  
205 anisotropy in interfacial energy. Second, some of the air cells tended to coalesce. One  
206 example is indicated by the arrows in Fig. 3(a) and (b), where two neighboring large  
207 air cells gradually merged into one.

208 Third, it is observed that during the heating stage the microstructural features  
209 moved to the upper right corner of the region in Fig. 3, and observed more clearly in  
210 supplementary Fig. S1, because of the volume shrinkage when ice crystals were  
211 melted into the unfrozen matrix. An air cell in Fig. 3(b) (indicated by a red arrow)  
212 shows the example of this movement. Note that the microstructure seemed to be  
213 compressed slightly due to the decreasing volume. It is mentioned that the expansion  
214 of volume seemed to be less significant during cooling as compared to the reduction  
215 in volume upon heating. The degree of expansion and relative movement during  
216 cooling also suggests the unfrozen matrix is quite flexible in response to external  
217 thermal change at high temperatures.

218 Microstructures in the longitudinal section were extracted for further examination  
219 and the results are shown in supplementary Fig. S1. The microstructural features (e.g.  
220 ice crystals and air cells) move less in the sample axis direction as compared to that in  
221 the cross section (Fig. 3). In other words, flotation of air cells along the sample axis  
222 does not occur, or at least was not observed in this study. This observation suggests

223 that macro-fluid flow was largely inhibited due to the increased viscosity of the  
224 unfrozen matrix due to the stabilizers present in the ice cream samples, which would  
225 inhibit the mobility of air cells [14]. In addition, it is also difficult to identify if  
226 drainage, which can play an important role in the instability of the air structure at high  
227 temperature [14], occurred in this work. However, it is also mentioned that  
228 microscopic fluid flow in the channels within the unfrozen matrix probably still  
229 occurs which cannot be resolved by the technique used in this work.

230

### 231 **3.2 3D Ice crystal evolution**

232 The volume fraction of ice crystals was examined first (Fig. 1), together with the  
233 calculated data based on the thermal properties (i.e. extrapolated melting points at  
234 various concentrations) of the ice cream formulation. Generally, the results measured  
235 by tomography compare well with the theoretical predictions. Minor errors might be  
236 caused by shrinkage and expansion, which would change some of the features  
237 measured.

238 Fig. 4 shows the 3D evolution of ice crystals during a thermal cycle. Ice crystals  
239 are individually color-rendered according to the equivalent diameter of each ice  
240 crystal. In the figure, the blue color corresponds to small size. As expected, ice  
241 crystals gradually decreased in size when the sample was heated, reaching the  
242 minimum size at  $-5\text{ }^{\circ}\text{C}$ . This is consistent with the observation that more small blue  
243 ice crystals were present at  $-5\text{ }^{\circ}\text{C}$ , as shown in Fig. 4(c). The ice crystals then  
244 continuously grew in size when the sample was cooled again to  $-15\text{ }^{\circ}\text{C}$  (Fig. 4(d-e)).

245 Detailed examination of the position change for the 3D ice crystals after heating  
246 shows that the ice crystals moved upwards slightly, by less than 20  $\mu\text{m}$ . This  
247 movement of the ice crystals might be caused by compression due to volume  
248 shrinkage, which drives the ice crystals to move upwards towards the center of the  
249 sample when the unfrozen matrix is less viscous at warmer temperatures [34].

250 The ice crystals in Fig. 4 were quantified in terms of equivalent diameter and size  
251 distribution (Fig. 5). The average equivalent diameter of ice crystals decreases upon  
252 heating from 101  $\mu\text{m}$  at  $-15\text{ }^{\circ}\text{C}$  to 87  $\mu\text{m}$  at  $-5\text{ }^{\circ}\text{C}$ , and then increases again to  $\sim 103\text{ } \mu\text{m}$   
253 at  $-15\text{ }^{\circ}\text{C}$  after cooling (Fig. 5(a)). Interestingly, the average equivalent diameter of the  
254 ice crystals is increased by  $\sim 2\text{ } \mu\text{m}$  at  $-15\text{ }^{\circ}\text{C}$  after a thermal cycle (Fig. 5(a)),  
255 suggesting a mild coarsening of ice crystals after thermal cycling. This coarsening of  
256 ice crystals at a storage temperature (e.g.  $-5\text{ } \sim -18\text{ }^{\circ}\text{C}$ ) with imposed oscillation  
257 temperatures (e.g.  $\pm 2.5\text{ }^{\circ}\text{C}$ ) have been previously observed [10, 23, 35, 36]. It is  
258 pointed out that the performed thermal cycling in this study leads to much higher  
259 coarsening rates than isothermal storage at a certain temperature due to the  
260 temperature oscillations which, through observed melting-recrystallization process,  
261 increases the rate of the coarsening process [23].

262 The size distribution of the ice crystals at different temperatures was analyzed  
263 and the results are plotted in Fig. 5(b-d). In general, the size distribution curves reflect  
264 the temperature change, where the curves shift to the left upon heating (Fig. 5(c)),  
265 while they shift to the right during the cooling stage (Fig. 5(d)). It is also shown in Fig.  
266 5(b) that the distribution of the two curves at  $-15\text{ }^{\circ}\text{C}$ , before and after the thermal

267 cycle, is similar indicating only a minor change in the overall size after the thermal  
268 cycle was completed. This observation confirms that the ice crystals follow mainly a  
269 “melting-recrystallization” mechanism and that other proposed mechanisms [37] play  
270 a small or negligible role.

271 Fig. 6 shows the morphological evolution of five individually separated ice  
272 crystals extracted for detailed examination. The morphology of the ice crystals  
273 changed during thermal cycling being more irregular at low temperature, e.g.  $-15\text{ }^{\circ}\text{C}$   
274 (Fig. 6(a) and (f)), while they became more spherical at “high” temperature, e.g.  $-5\text{ }^{\circ}\text{C}$   
275 (Fig. 6(c) and (d)).

276 The five ice crystals shown in Fig. 6 are quantified in terms of volume, volume  
277 change, specific surface area and sphericity, and the results are presented in Fig. 7. It  
278 is seen that the volume of each ice crystal keeps decreasing during heating and then  
279 increasing during cooling. The volume change (as compared to  $-15\text{ }^{\circ}\text{C}$  before thermal  
280 cycling) shows that the volume of four of the ice crystals increased by 5.5-11%,  
281 indicating an increase in size of ice crystals, which is consistent with the observation  
282 of the overall increased equivalent diameter of ice crystals due to coarsening (Fig.  
283 5(a)). However, the volume of ice crystal 3 decreased slightly, by  $\sim 4\%$ . This ice  
284 crystal is one of the smallest of the 5, and most likely the other four ice crystals grew  
285 at the expense of ice crystal 3 via an Ostwald Ripening mechanism [37].

286 In this study, complete melting of ice crystals was not observed when the sample  
287 was heated to  $-5\text{ }^{\circ}\text{C}$  since the smallest crystals will have dissolved in the seven  
288 thermal cycles prior to the *in situ* experiment. After seven cycles the ice crystals have

289 grown to a large enough size such that they don't completely melt during heating to -5  
290 °C. This critical size can be extracted from Fig. 5(b). Note that the smallest crystals  
291 measured are about 60  $\mu\text{m}$  diameter at -15 °C, and reduce in size by  $\sim 25 \mu\text{m}$  when  
292 heated to -5 °C. This observation suggests that ice crystals with an equivalent  
293 diameter less than 25  $\mu\text{m}$  have a high probability of being completely melted during  
294 the applied thermal cycling. This is further supported by the observation that there is  
295 no significant number of crystals less than 30  $\mu\text{m}$  diameter at -5 °C. This finding  
296 confirms the measurements made in a previous study by the same authors (i.e. Fig.  
297 9(d) in ref. [5]) showing a significant reduction in the number of ice crystals during the  
298 first 7 cycles.

299 As mentioned, the morphology of ice crystals also changes during thermal  
300 cycling (Figs. 3 and 6). This change is quantified using measures of specific surface  
301 area and sphericity in Fig. 7 (c) and (d). For example, both the values of specific  
302 surface area and sphericity increased continuously as the ice crystals melt, decreasing  
303 as the ice crystals recrystallized. These changes support the observation that ice  
304 crystals become more spherical during melting (to minimize interfacial energy) and  
305 then became more faceted (irregular) during the recrystallization stage as they strive  
306 to reach the Wulff shape driven by anisotropy in interfacial energy [38, 39]. However,  
307 the ice crystals show only minor morphological changes after a thermal cycle, as  
308 indicated by the average sphericity of more than 300 ice crystals where the value  
309 increased from  $\sim 0.80$  at -15 °C to 0.84 at -5 °C during the heating stage, and then  
310 decreased to  $\sim 0.80$  when cooled back to -15 °C. A similar trend was observed for the

311 specific surface area. The minor changes to the size and morphology of ice crystals  
312 after one thermal cycle support the previous findings that only small differences in  
313 size and morphology of ice crystals were observed between the sample thermally  
314 cycled for 7 days and the sample cycled for 14 days [5].

### 315 **3.3 Unfrozen matrix evolution**

316 Fig. 8 and supplementary Fig. S2 (larger volume) show the 3D morphological  
317 evolution of the unfrozen matrix during a thermal cycle. The unfrozen matrix forms a  
318 very complex 3D network-like shape with ice crystals and air bubbles dispersed  
319 within the matrix. The 3D images in Fig. 8(a-f) show that the unfrozen matrix  
320 appeared thicker between air cells upon heating, while they became thinner as the  
321 sample cooled down presumably due to the melting of the ice crystals during heating  
322 and recrystallization during cooling. This is reflected by the quantified thickness of  
323 the unfrozen matrix analyzed in a  $721 \times 721 \times 504 \mu\text{m}^3$  volume (supplementary Fig. S2),  
324 as plotted in Fig. 8(g) where the thickness monotonically increased from  $\sim 12.6 \mu\text{m}$  at  
325  $-15^\circ\text{C}$  to  $27.0 \mu\text{m}$  at  $-5^\circ\text{C}$ , and then decreased to  $\sim 19.6 \mu\text{m}$  at  $-15^\circ\text{C}$  at the end of the  
326 thermal cycle.

327 Figure 8 shows that the thickness of the unfrozen matrix is greater during the  
328 cooling stage than during the heating stage, such that the thickness increases by  $\sim 6$   
329  $\mu\text{m}$  after the thermal cycle was completed. After detailed examination, it is  
330 hypothesised that the formation of a local region of the matrix (e.g. upper right corner  
331 in Fig. 3) that is concentrated with more water molecules, is responsible for this  
332 change. The shrinkage of the sample, and the associated macro-flow induced by the

333 compression effect, might have accelerated the formation of a larger region of low  
334 viscosity matrix. During the cooling stage, no additional new ice crystals were  
335 nucleated under the cooling rate studied. Thus, the measured thickness of the unfrozen  
336 matrix in this region is higher compared to that before thermal cycling.

337 In addition, the 'strength' (or viscosity) of the unfrozen matrix would decrease at  
338 the higher temperatures during heating due to a reduction in viscosity allowing more  
339 movement of the matrix to accommodate the overall shrinkage of the sample (see  
340 above). Thus, a shift of the structure was observed during the heating stage,  
341 suggesting a significant negative impact of the ice melting process on structural  
342 stability.

343

#### 344 **3.4 3D air cell evolution**

345 A few 3D air cells were extracted to examine the coarsening mechanism. Fig. 9  
346 shows one example where two separate air cells gradually merge into one. It is  
347 observed that the air cells at  $-15^{\circ}\text{C}$  are not necessarily round, instead, they have many  
348 concave regions (indicated by an arrow in Fig. 9(a)), or even an elongated shape for  
349 some cases as seen in Fig. 3. Upon heating, the two air cells merged by creating a  
350 bridge between them (Fig. 9(b)), and then the bridge (or neck) continued to thicken  
351 with increasing temperature during the heating stage. Meanwhile, some of the  
352 concave regions on the air cell surface gradually disappear forming a smooth or  
353 spherical surface. The gradual rounding was driven by the reduction in surface energy  
354 of the air/unfrozen matrix interface [40].



355        Decreased viscosity of the unfrozen matrix at “warmer” temperatures upon  
356 heating increases the diffusion rate of gas between air cells and promotes coalescence  
357 of air cells. It is mentioned that adding stabilizers and emulsifier to ice cream helps  
358 reduce air cell coarsening, due to the increased extent of fat destabilization and the  
359 increased viscosity of the matrix phase, respectively [14]. It is also noticed that the  
360 surrounding ice crystals significantly affect the shape of the area around the neck  
361 between merging cells. One example is shown in Fig. 9(d-2). It is likely that those ice  
362 crystals in the vicinity of the neck limit further coalescence of the two air cells due to  
363 the constraint imposed by the ice crystal imbedded unfrozen matrix (also see  
364 supplementary Fig. S3).

365        Upon cooling, some of the phenomena observed during the heating stage act in  
366 reverse. That is, the surface of air cells became rough or even distorted again at  
367 “cooler” temperatures, e.g. -12 °C in Fig. 9(g). This is most obvious at the lowest  
368 temperature of -15 °C (Fig. 9(h) and (h-2)). The changes are likely to be caused by  
369 two main factors. One is that the growing ice crystals continue to push towards the air  
370 cells through the unfrozen matrix. This is realized more easily when the unfrozen  
371 matrix becomes thinner and thinner as more water molecules are attached to the  
372 recrystallizing ice crystals. In total, twenty ice crystals were observed to grow around  
373 the air cells shown in Fig. 9 (see supplementary Fig. S3). The second factor is that the  
374 pressure within the air cell decreases with the decreasing temperature according to the  
375 ideal gas law ( $PV=nRT$ ), releasing some of the force on the surface that resists  
376 morphological change. It is mentioned that the final morphological change is a result

377 of competition between the force imposed on the air cell surface by the growing ice  
378 crystals and the surface tension of the air cell/matrix interface. It seems that for the  
379 case in Fig. 9 the force imposed by the growing ice crystals through the matrix was  
380 greater than the surface tension at temperatures lower than  $\sim -12$  °C, under which the  
381 surface started to deform significantly. In addition, the coalescence process seemed to  
382 be inhibited by the increased viscosity at low temperatures during the cooling stage,  
383 indicating a significantly reduced rate of morphological change of the air cells than  
384 during the heating stage.

385 Pelan et al. [41] and Rohenkohl and Kohlus [42] both suggested that the  
386 coalescence of air cells to create large coarsened air pockets was the major  
387 destabilizing mechanism in the ice cream they studied. A previous study revealed that  
388 the storage of ice cream without emulsifier or stabilizer at  $-15$  °C for 16 days lead to  
389 interconnected channels [14]. The recent observations by Guo et al. [5] also showed  
390 that thermal cycling of ice cream between  $-15$  and  $-5$  °C for 14 days resulted in a very  
391 complex interconnected air structure [5]. Although Ostwald ripening was observed in  
392 the aerated emulsions [43], the *in situ* observations in this study strongly suggest that  
393 for ice cream that was cycled for seven times coalescence is the dominant mechanism  
394 responsible for the creation of complex interconnected air structures. It should be  
395 noted that gas formation can occur due to radiation damage, resulting in molecular  
396 bond cleavage (H-H and O-O) or water photolysis, as reported in water under high  
397 pressures [44]. If this is occurring, it could explain the increase in bubble volume  
398 fraction and the coarsening of bubbles. However, the increase in bubble volume will

399 not have a significant impact on the coarsening of the ice crystals. Gas formation due  
400 to irradiation is an open question, as is how this might affect bubble coarsening.

401 Apart from the coarsening of air cells, another interesting phenomenon was  
402 observed, i.e. the reduced volume of some of the air cells after thermal cycling. Fig.  
403 10 shows the evolution of three individually extracted air cells during thermal cycling,  
404 and their corresponding quantified volume changes are plotted in Fig. 11. The overall  
405 volume fraction of air cells was also analyzed and the result was observed to decrease  
406 monotonically during the heating stage, and continued to decrease until 0.256 at  $\sim -7$   
407  $^{\circ}\text{C}$  during cooling before it started to rise upon further freezing (Fig. 11(a)). The  
408 volume fraction after the thermal cycle ( $\sim 0.285$ ) was lower compared to that before  
409 thermal cycling began ( $\sim 0.330$ ). This corresponds to a reduction of volume fraction  
410 by  $\sim 13.8\%$ . The trend of the volume change of the three individual air cells is  
411 consistent with that for the overall volume change. It is also noticed that the change of  
412 volume is even more than 50% for Air 2 and Air 3, and that those two air cells did not  
413 grow in size during the cooling stage. Detailed mechanisms here are still unknown. It  
414 is unlikely that the hydrostatic pressure causes such a large change, as the sample  
415 height is quite small. The shift of the sample during the thermal cycle might  
416 contribute to some measurement errors; however, the volume (thus size) change of the  
417 air cells is proposed to be the main contribution, which is supported by the volume  
418 change of all three air cell cases (Fig. 11(c-d)). The diffusion of gas into the matrix  
419 and the surrounding air cells, as well as out of the whole sample, at the warm

420 temperatures might have contributed to this change. The detailed mechanisms will be  
421 investigated in a future study.

422

### 423 **3.5 Summary of microstructural evolution mechanisms**

424 Here, the mechanisms that control the microstructural evolution of ice cream as  
425 observed in this *in situ* study are summarised (Table 1). Generally, the microstructural  
426 evolution of ice cream during thermal cycling is controlled by the interaction of three  
427 phases.

428 Regarding ice crystals, nucleation of new ice crystals does not occur under the  
429 cooling condition studied in this work. The melting-recrystallization mechanism  
430 hypothesized as an important mechanism in the previous study by Guo et al. [5] was  
431 quantified by analyzing the 4-D tomographs during the thermal cycle. The melting  
432 and recrystallization of ice crystals also affects the air cell's morphology, as well as  
433 its coarsening process, through the unfrozen matrix layer between the ice crystals and  
434 the air structures. For the air phase, coalescence of air cells is clearly observed to be  
435 responsible for the coarsening mechanism. For the sample that was initially thermally  
436 cycled for seven times, Ostwald ripening takes a less important role in the coarsening  
437 of both ice crystals and air cells during thermal cycling. The continuous reduction of  
438 air cell volume needs further investigation. The third phase, the unfrozen matrix, is a  
439 crucial component controlling the microstructural stability of ice cream. It acts as the  
440 reservoir for the water from dissolving ice during heating and releases water for  
441 recrystallization of the ice crystals during the cooling cycle. The network of unfrozen  
442 matrix, reinforced by the distributed ice crystals (and dissolved hydrocolloids), holds

443 the whole structure together and greatly influences the structural stability of ice cream  
444 when subjected to external temperature variations.

445

#### 446 **4. Conclusions**

447 Using 4D synchrotron X-ray tomography, the effect of thermal variation on the  
448 microstructural stability of ice cream was investigated during a heating and cooling  
449 cycle between -15 °C and -5 °C, at a ramp rate of 0.05 °C/min. A new data  
450 reconstruction and image processing method was developed, enabling the large 4D  
451 data sets to be segmented and quantified. The experimental set-up, as well as the  
452 image processing routine developed, can be applied to a wide range of soft materials.

453 The dynamic evolution of individual microstructural features, i.e. an ice crystal,  
454 air cell, and unfrozen matrix, was quantitatively analyzed. The findings integrate the  
455 *ex situ* observations made in Guo et al. [5] enhancing the understanding of the  
456 mechanisms controlling ice cream's microstructural evolution. The experimental  
457 results in this study reveal important physical mechanisms that influence  
458 microstructural instability: that is, the coarsening of air cells takes place mainly  
459 through the coalescence of neighboring air cells, while ice crystal growth results from  
460 the melting-recrystallization mechanism during thermal cycling, both of which lead to  
461 degradation of ice cream's microstructure. The unfrozen matrix plays an important  
462 role in maintaining the integrity of the structure of ice cream while being flexible  
463 enough at the higher temperatures to reduce the stresses imposed during heating and  
464 then cooling by the melting and recrystallization of the ice crystals.

465

466 **Acknowledgements**

467 This work was financially supported by Unilever R&D (Colworth, U. K) and in  
468 part by the EPSRC (EP/I02249X/1, EP/J010456/1 and EP/M009688/1). The authors  
469 acknowledge the use of the facility access in Diamond Light Source (MT12194,  
470 MT12195 & MT12616) and Research Complex at Harwell. The authors also thank  
471 I13 staff of Diamond Light Source (especially Drs. Rau, Wanelik, Cipiccia and  
472 Marathe) and group members for technical support.

473 **Data statement**

474 Representative samples of the research data are shown in the figures. Other  
475 datasets generated during and/or analysed during this study are not publicly available  
476 due to their large size but are available from the corresponding author on reasonable  
477 request.

478

479 **References**

- 480 [1] R.G.M. van der Sman, A.J. van der Goot, The science of food structuring, *Soft*  
481 *Matter* 5(3) (2009) 501-510.
- 482 [2] J. Ubbink, A. Burbidge, R. Mezzenga, Food structure and functionality: a soft  
483 matter perspective, *Soft Matter* 4(8) (2008) 1569-1581.
- 484 [3] A. Kovalenko, K. Zimny, B. Mascaro, T. Brunet, O. Mondain-Monval, Tailoring  
485 of the porous structure of soft emulsion-templated polymer materials, *Soft Matter*  
486 12(23) (2016) 5154-5163.
- 487 [4] B. R. Pinzer, A. Medeback, H. J. Limbach, C. Dubois, M. Stampanoni and M.  
488 Schneebeil, 3D-characterization of three-phase systems using X-ray tomography:  
489 tracking the microstructural evolution in ice cream, *Soft Matter*, 4584 (8) (2012)  
490 4584-4594.
- 491 [5] E.Y. Guo, G. Zeng, D. Kazantsev, P. Rockett, J. Bent, M. Kirkland, G. Van Dalen,  
492 D.S. Eastwood, D. StJohn, P.D. Lee, Synchrotron X-ray tomographic quantification of  
493 microstructural evolution in ice cream - a multiphase soft solid, *RSC Advances* 7(25)  
494 (2017) 15561-15573.
- 495 [6] G.V. Dalen, A study of bubbles in foods by X-ray microtomography and image  
496 analysis, *Microscopy and Analysis* 26(2) (2012) S8-S12.

- 497 [7] C. Clarke, *The Science of Ice Cream*, CPI Group (UK) Ltd, Croydon, UK , 2012.
- 498 [8] H. Matthias D. Eisner, E.J. Windh, Air cell microstructuring in a high viscous ice  
499 cream matrix, *Colloids and Surfaces A: Physicochem. Eng. Aspects* 263 (2005)  
500 390-399.
- 501 [9] A.P. Paula Varela, S. Fiszman, How hydrocolloids affect the temporal oral  
502 perception of ice cream, *Food Hydrocolloids* 36 (2014) 220-228.
- 503 [10] M. Tsevdou, E. Gogou, E. Dermesonluoglu, P. Taoukis, Modelling the effect of  
504 storage temperature on the viscoelastic properties and quality of ice cream, *Journal of*  
505 *Food Engineering* 148 (2015) 35-42.
- 506 [11] J.J. Cheng, J. Cui, Y. Ma, T.S. Yan, L.F. Wang, H. Li, X.S. Li, Effects of  
507 soy-to-milk protein ratio and sucrose fatty acid ester addition on the stability of ice  
508 cream emulsions, *Food Hydrocolloids* 60 (2016) 425-436.
- 509 [12] J.V. Patmore, H.D. Goff, S. Fernandes, Cryo-gelation of galactomannans in ice  
510 cream model systems, *Food Hydrocolloids* 17(2) (2003) 161-169.
- 511 [13] A. Regand, H.D. Goff, Structure and ice recrystallization in frozen stabilized ice  
512 cream model systems, *Food Hydrocolloids* 17 (2003) 95-102.
- 513 [14] Y. Chang, R.W. Hartel, Stability of air cells in ice cream during hardening and  
514 storage, *Journal of Food Engineering* 55 (2002) 59-70.
- 515 [15] K.L.K. Cook, R.W. Hartel, Effect of freezing temperature and warming rate on  
516 dendrite break-up when freezing ice cream mix, *International Dairy Journal* 21 (2011)  
517 447-453.
- 518 [16] Y. Chang, R.W. Hartel, Development of air cells in a batch ice cream freezer,  
519 *Journal of Food Engineering* 55 (2002) 71-78.
- 520 [17] A. Caillet, C. Cogne, J. Andrieu, P. Laurent, A. Rivoire, Characterization of ice  
521 cream structure by direct optical microscopy. Influence of freezing parameters,  
522 *Lebensmittel-Wissenschaft Und-Technologie-Food Science and Technology* 36(8)  
523 (2003) 743-749.
- 524 [18] J.J. Cheng, Y. Ma, X.S. Li, T.S. Yan, J. Cui, Effects of milk  
525 protein-polysaccharide interactions on the stability of ice cream mix model systems,  
526 *Food Hydrocolloids* 45 (2015) 327-336.
- 527 [19] E. Faydi, J. Andrieu, P. Laurent, Experimental study and modelling of the ice  
528 crystal morphology of model standard ice cream. Part I: Direct characterization  
529 method and experimental data, *Journal of Food Engineering* 48 (2001) 283-291.
- 530 [20] K.B. Caldwell, H.D. Goff, D.W. Stanley, R.W. Martin, A low-temperature  
531 scanning electron microscopy study of ice cream. 1. Techniques and general  
532 microstructure, *Food Structure* 11(1) (1992) 1-9.
- 533 [21] A.A. Flores, H.D. Goff, Ice crystal size distributions in dynamically frozen model  
534 solutions and ice cream as affected by stabilizers, *Journal of Dairy Science* 82(7)  
535 (1999) 1399-1407.
- 536 [22] C. Mendez-Velasco, H.D. Goff, Fat structure in ice cream: A study on the types  
537 of fat interactions, *Food Hydrocolloids* 29(1) (2012) 152-159.
- 538 [23] F.T. Ndoye, G. Alvarez, Characterization of ice recrystallization in ice cream  
539 during storage using the Focused Beam Reflectance Measurement, *Journal of Food*  
540 *Engineering* 148 (2015) 24-34.

- 541 [24] E.Y. Guo, A.B. Phillion, B. Cai, S.S. Shuai, D. Kazantsev, T. Jing, P.D. Lee,  
542 Dendritic evolution during coarsening of Mg-Zn alloys via 4D synchrotron  
543 tomography, *Acta Materialia* 123 (2017) 373-382.
- 544 [25] K.M. Kareh, P.D. Lee, R.C. Atwood, T. Connolley, C.M. Gourlay, Revealing the  
545 micromechanisms behind semi-solid metal deformation with time-resolved X-ray  
546 tomography, *Nature Communications* 5 (2014).
- 547 [26] S. Karagadde, P.D. Lee, B. Cai, J.L. Fife, M.A. Azeem, K.M. Kareh, C.  
548 Puncreobutr, D. Tsivoulas, T. Connolley, R.C. Atwood, Transgranular liquation  
549 cracking of grains in the semi-solid state, *Nature Communications* 6 (2015).
- 550 [27] P. Rockett, S. Karagadde, E. Guo, J. Bent, J. Hazekamp, M. Kingsley, J.  
551 Vila-Comamala, P.D. Lee, A 4-D dataset for validation of crystal growth in a complex  
552 three-phase material, ice cream, IOP conf. series: Materials science and engineering,  
553 84(2015) 012076.
- 554 [28] A.C. Kak, M. Slaney, Principles of computerized tomographic imaging, IEEE  
555 Press, New York, 2001.
- 556 [29] D. Kazantsev, F. Bleichrodt, T. Van Leeuwen, A. Kaestner, P. Withers, K.J.  
557 Batenburg, P.D. Lee, A novel tomographic reconstruction method based on the robust  
558 Student's t function for suppressing data outliers, *IEEE Transactions on*  
559 *Computational Imaging* 99 (2017) 1-1.
- 560 [30] D. Kazantsev, E.Y. Guo, A.B. Phillion, P.J. Withers, P.D. Lee, Model-based  
561 iterative reconstruction using higher-order regularization of dynamic synchrotron data,  
562 *Measurement Science and Technology* 28(9) (2017).
- 563 [31] P. Paleo, A. Mirone, Ring artifacts correction in compressed sensing tomographic  
564 reconstruction, *Journal of Synchrotron Radiation* 22 (2015) 1268-1278.
- 565 [32] J. Weickert, Anisotropic diffusion in image processing, Stuttgart: Teubner, 1998.
- 566 [33] M. Doube, M.M. Klosowski, I. Arganda-Carreras, F.P. Cordelieres, R.P.  
567 Dougherty, J.S. Jackson, B. Schmid, J.R. Hutchinson, S.J. Shefelbine, BoneJ Free and  
568 extensible bone image analysis in ImageJ, *Bone* 47(6) (2010) 1076-1079.
- 569 [34] H.D. Goff, R.W. Hartel, Ice cream, 7th Edition ed., Springer Science & Business  
570 Media, New York, 2013.
- 571 [35] D.P. Donhowe, R.W. Hartel, Recrystallization of ice in ice cream during  
572 controlled accelerated storage, *International Dairy Journal* 6(11-12) (1996)  
573 1191-1208.
- 574 [36] D.P. Donhowe, R.W. Hartel, Recrystallization of ice during bulk storage of ice  
575 cream, *International Dairy Journal* 6(11-12) (1996) 1209-1221.
- 576 [37] K.L.K. Cook, R.W. Hartel, Mechanisms of Ice Crystallization in Ice Cream  
577 Production, *Comprehensive Reviews in Food Science and Food Safety* 9(2) (2010)  
578 213-222.
- 579 [38] G. Wulff, On the question of speed of growth and dissolution of crystal surfaces,  
580 *Zeitschrift Fur Krystallographie Und Mineralogie* 34(5/6) (1901) 449-530.
- 581 [39] R. Shuttleworth, The surface tension of solids, *Proceedings of the Physical*  
582 *Society of London Section A* 63(365) (1950) 444-457.
- 583 [40] P. Walstra, Dispersed systems: basic consideration, in: O.R. Fennema (Ed.)  
584 Marcel Dekker., New York, 1996, pp. 95-115.



- 585 [41] B.M.C. Pelan, K.M. Watts, I.J. Campbell, A. Lips, The stability of aerated milk  
586 protein emulsions in the presence of small molecule surfactants, *Journal of Dairy*  
587 *Science* 80(10) (1997) 2631-2638.
- 588 [42] H. Rohenkohl, R. Kohlus, Foaming of ice cream and the time stability of its  
589 bubble size distribution, in: G.M. Campbell, C. Webb, S. Pandiello, K. Niranjana (Eds.)  
590 *Bubbles in food*, MN: Eagan Press., 1999, pp. 45-53.
- 591 [43] G.V. Dalen, M.W. Koster,  $\mu$ CT imaging of aerated emulsions, SkyScan user  
592 meeting, Leuven, Belgium, 2011.
- 593 [44] W.L. Mao, H.K. Mao, Y. Meng, P.J. Eng, M.Y. Hu, P. Chow, Y.Q. Cai, J.F. Shu,  
594 R.J. Hemley, X-ray-induced dissociation of H<sub>2</sub>O and formation of an O-2-H-2 alloy at  
595 high pressure, *Science* 314(5799) (2006) 636-638.
- 596
- 597

598

599 **Figure captions**

600 Fig. 1 Change in ice volume fraction as a function of temperature. The inset shows the  
601 thermal cycling history of the ice cream sample for the *in situ* synchrotron  
602 experiment. The measured phase diagram (i.e. extrapolated melting points at various  
603 concentrations) of the ice cream formulation is presented in [5].

604

605 Fig. 2 Reconstructed images using (a) conventional FBP reconstruction method and (b)  
606 MBIR reconstruction method; (c) post-processed image of reconstructed MBIR image  
607 of (b), note more homogeneous (equalized) intensities compared to (b) within  
608 ice-crystals; (d) 3-phases segmentation using (c). A, I and M in (b) stand for air cell,  
609 ice crystal and unfrozen matrix, respectively. Scale bar =150  $\mu\text{m}$ .

610

611 Fig. 3 Reconstructed tomographic slices (prior to the equalization step) showing the  
612 overall microstructural evolution of ice cream during a thermal cycle: (a) -15  $^{\circ}\text{C}$ , (b)  
613 -7.6  $^{\circ}\text{C}$ , and (c) -5  $^{\circ}\text{C}$  during heating, (d) after holding at -5  $^{\circ}\text{C}$  for 10 min, (e) -7.5  $^{\circ}\text{C}$ ,  
614 and (f) -15  $^{\circ}\text{C}$  during refreezing. A, I and M in (f) stand for air cell, ice crystal and  
615 unfrozen matrix, respectively. Scale bar equals 150  $\mu\text{m}$ .

616

617 Fig. 4 3D ice crystal evolution in a  $1416 \times 1416 \times 504 \mu\text{m}^3$  volume during a thermal  
618 cycle: (a) -15  $^{\circ}\text{C}$ , (b) -7.6  $^{\circ}\text{C}$ , (c) -5  $^{\circ}\text{C}$ , (d) -7.5  $^{\circ}\text{C}$ , and (e) -15  $^{\circ}\text{C}$ . Ice crystals are  
619 size-colored using the equivalent diameter. Scale bar equals 500  $\mu\text{m}$ .

620

621 Fig. 5 Quantified ice crystal size during a thermal cycle: (a) change of average  
622 equivalent diameter of ice crystals during a thermal cycle; (b-d) size distribution of  
623 ice crystals during (b) a complete thermal cycle, (c) heating stage and (d) cooling  
624 stage. The arrow in (b) indicates the size shift of the curves. Note, more than 300 ice  
625 crystals were analyzed.

626

627 Fig. 6 3D morphological evolution of five ice crystals during a thermal cycle: (a) -15  
628 °C, (b) -7.6 °C, (c) -5 °C, (d) after holding at -5 °C for 10 min, (e) -7.5 °C, and (f) -15  
629 °C. The time is indicated in each figure during the thermal cycle. Scale bar 150  $\mu\text{m}$  for  
630 all images. Numbers in (c) match the ice crystals analyzed in Fig. 7.

631

632 Fig. 7 Quantified results of five ice crystals during a thermal cycle: (a) volume, (b)  
633 volume change, (c) specific surface area, and (d) sphericity. Note the colours of the  
634 plots in each figure are identical to the colour-rendered ice crystals in (b).

635

636 Fig. 8 3D morphological evolution of unfrozen matrix within a  $259 \times 243 \times 243 \mu\text{m}^3$   
637 volume during a thermal cycle: (a) -15 °C, (b) -7.6 °C, (c) -5 °C, (d) after holding at -5  
638 °C for 10 min, (e) -7.5 °C, and (f) -15 °C; (g) Average thickness of the unfrozen matrix  
639 as a function of temperature. Note, the thickness is measured within a  $721 \times 721 \times 504$   
640  $\mu\text{m}^3$  volume, identical to the domain as shown in supplementary Fig. S2. Figures (a-f)  
641 share the same scale bar. Scale bar equals 100  $\mu\text{m}$ .

642

643 Fig. 9 Coalescence of two air cells during the heating stage (a-d) and cooling stage  
644 (e-h) of a thermal cycle. (d-2) and (h-2) show the morphological relationship between  
645 the surrounding ice crystals and the air cell at -5 °C and -15 °C, respectively. Scale bar  
646 100  $\mu\text{m}$  for all images.

647

648 Fig. 10 Morphological evolution of three individual air cell cases during a thermal  
649 cycle. Scale bar 100  $\mu\text{m}$  for all images.

650

651 Fig. 11 Volume change of air cells as a function of temperature during a thermal cycle:  
652 (a) overall volume change of air cells in a  $1416 \times 1416 \times 504 \mu\text{m}^3$  volume, (b) volume  
653 change of three individual air cells.



654

655

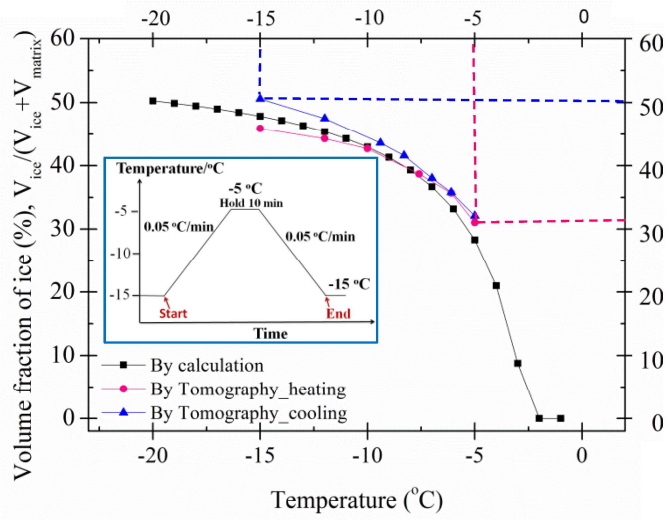
1 **Table**

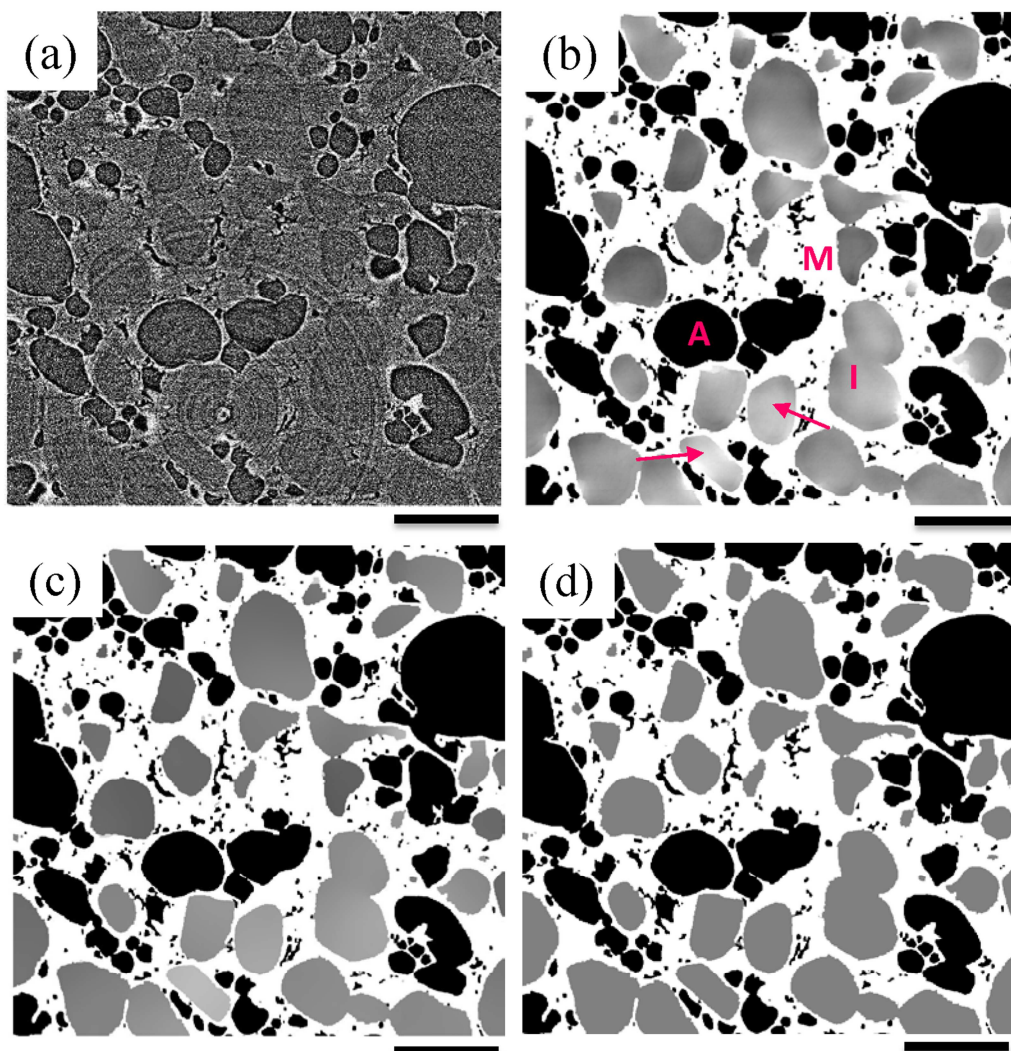
2

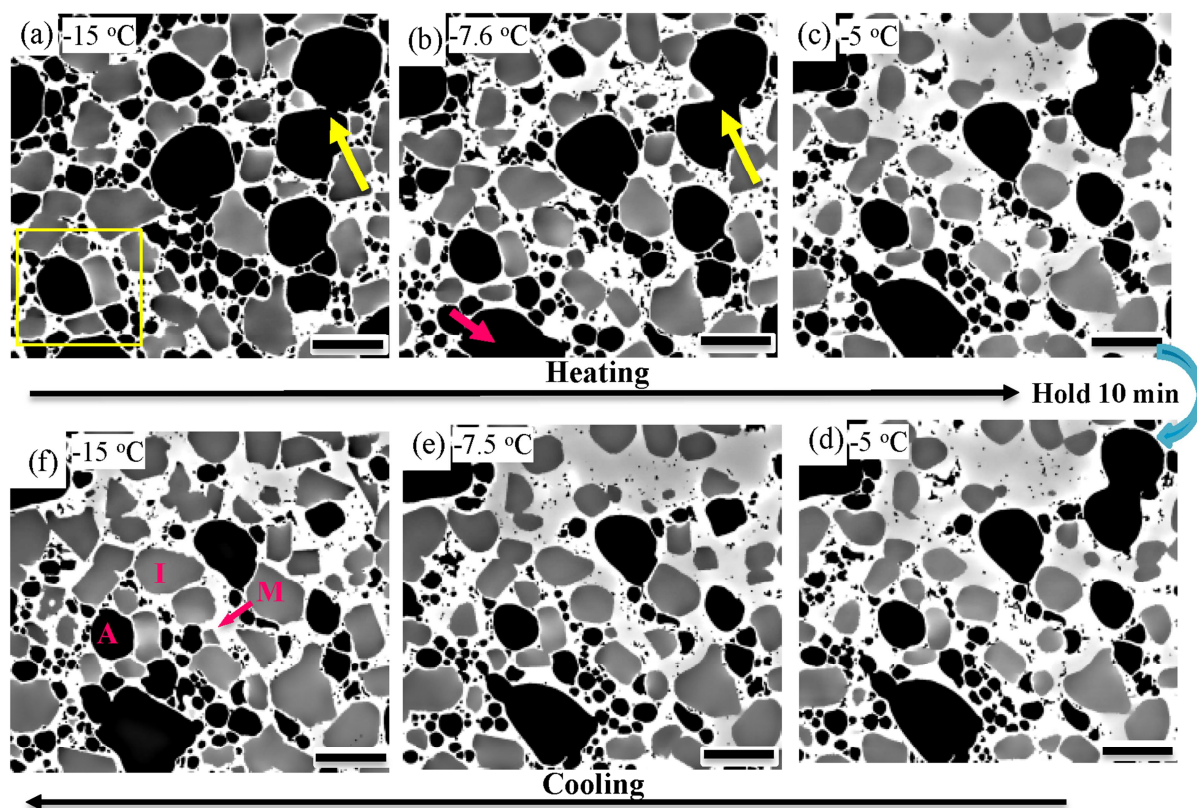
3 Table 1 A summary of the microstructural changes that occur during a thermal  
 4 cycling from -5 to -15 °C highlighting the differences between what occurs during the  
 5 first seven cycles and the following seven cycles. The arrows indicate that part of the  
 6 cycle over which most change occurs.

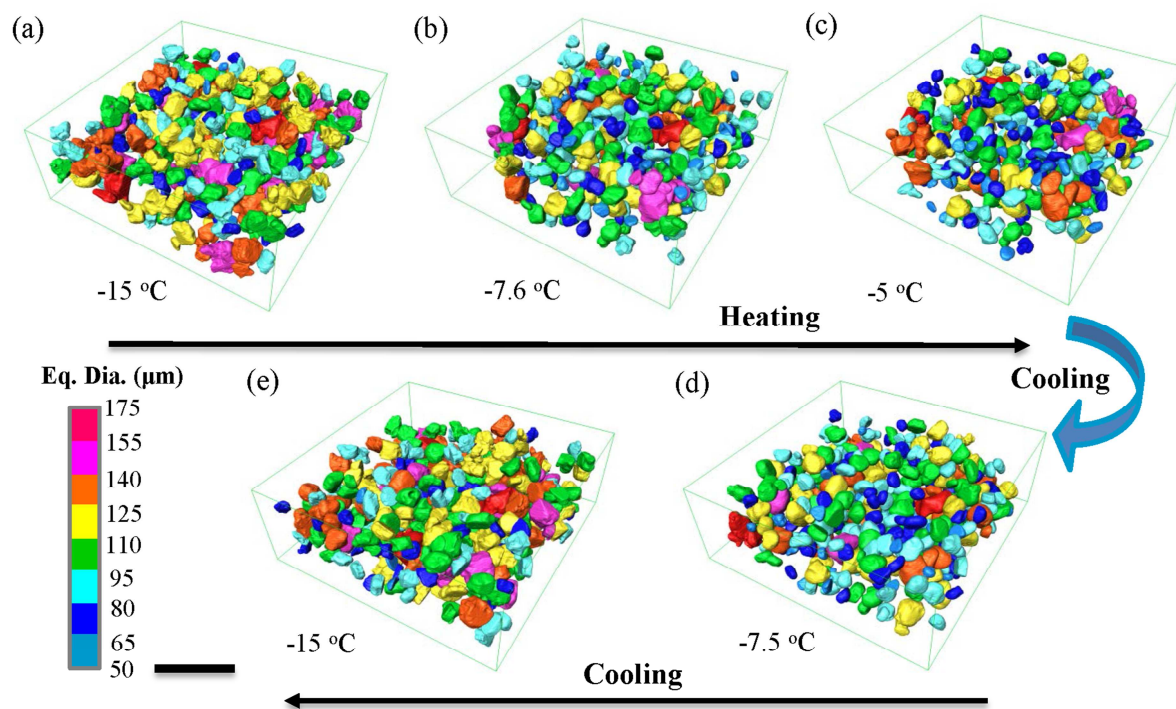
	Heat to -5 °C	Hold at -5 °C	Cool to -15 °C	Hold at -15 °C
<b>Air cells</b>				
Coalescence of neighbouring air cells. 				
1 to 7 cycles	Size increases although some small air cells remain leading to a bimodal distribution and remain equiaxed.		The air cells shrink.	Cells remain relatively spherical.
8 to 14 cycles	Coalescence of neighbouring air cells.		The air cells become irregular due to constraint by matrix and ice crystals.	Air cells become interconnected and form channels within the matrix network.
<i>Air cells continue to grow into a large interconnected network of irregular shapes as the number of thermal cycles increase. The morphology is constrained by the network of unfrozen matrix and ice crystals.</i>				
<b>Ice crystals</b>				
	Melt by ~40%		Grow by ~66%	
Dissolution  Recrystallization				
1 to 7 cycles	Size of ice crystals decrease and those < 25 µm melt completely. The morphology becomes rounded.	The size and morphology of crystals change little.	Size of ice crystals increase and no nucleation of new crystals occurs. The morphology becomes irregular during recrystallization.	Over the cycle, the size increases significantly and the number decrease significantly.
8 to 14 cycles	Size decreases by ~ 25 µm dissolving and the number changes little.	The size of crystals change little.	Size of ice crystals increase by about 25 µm. The number remains unchanged.	Over the cycle, the size increases by a small amount and the number do not increase.
<i>After 7 thermal cycles, the number changes little and the size of ice crystals increase slowly. The ice crystals form networks within the unfrozen matrix network.</i>				
<b>Unfrozen matrix</b>				
Water content	Increases	High	Decreases	Low
Viscosity	Viscosity decreases	Low	Viscosity increases	High
Mechanical response	Matrix becomes and remains flexible, reducing residual stresses		Matrix becomes less flexible	Matrix is effectively rigid
Total volume	Ice cream expands	May shrink somewhat	Ice cream shrinks	Relatively constant
<i>Alignment of ice crystals with the unfrozen matrix network occurs to minimise surface energy and reduce local stress with each additional thermal cycle. At the warmer temperatures the matrix becomes flexible also reducing stresses developed by the constraint of ice crystal and air cells.</i>				

7

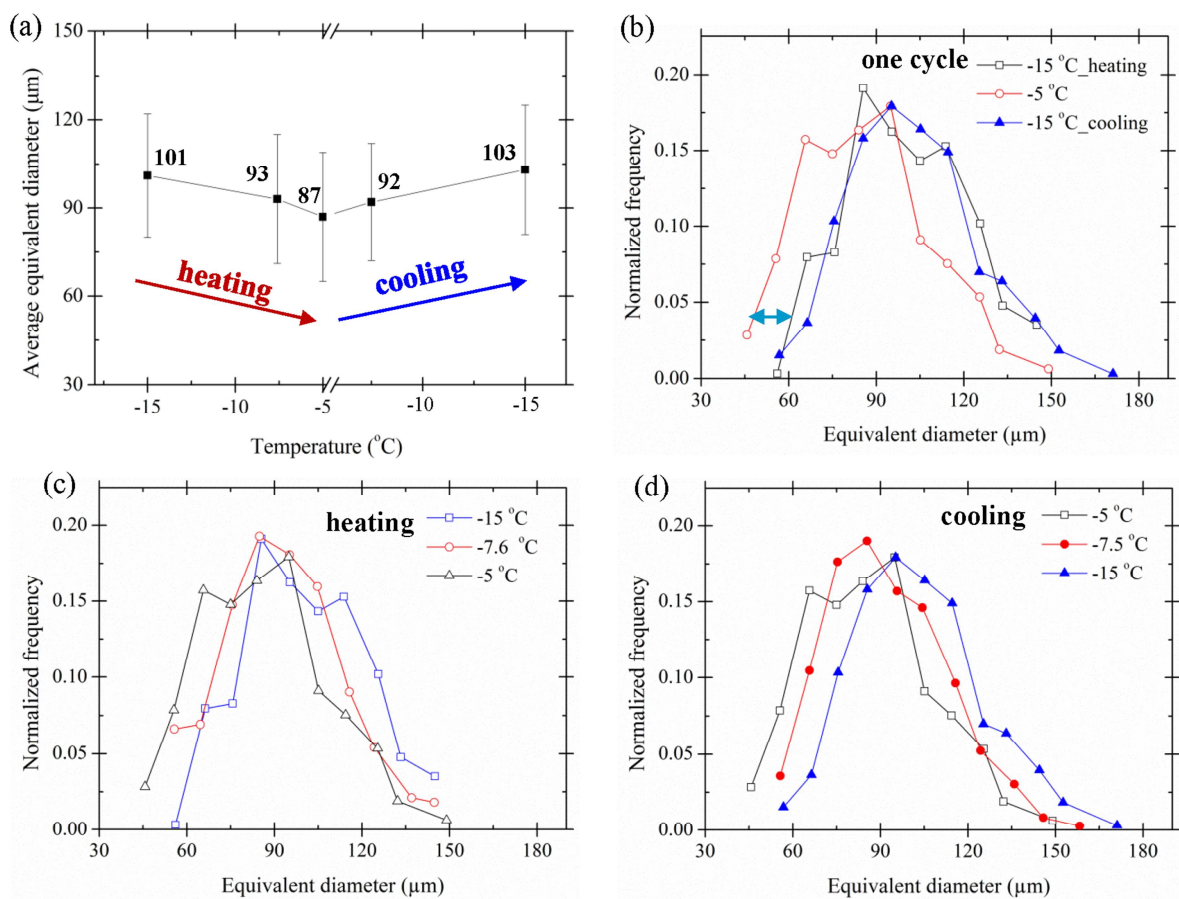


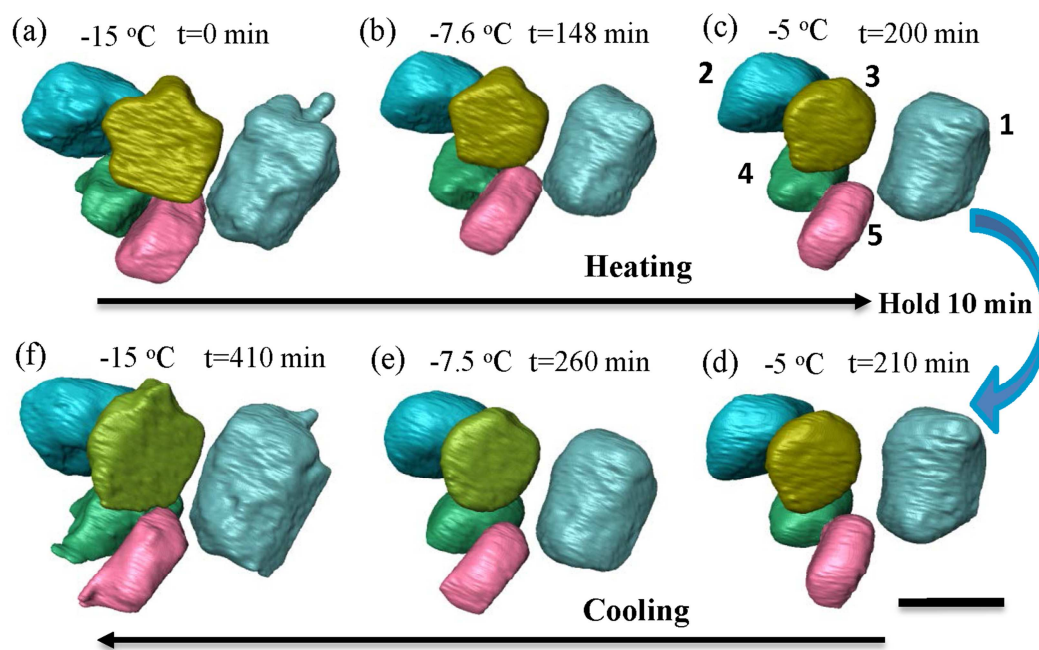


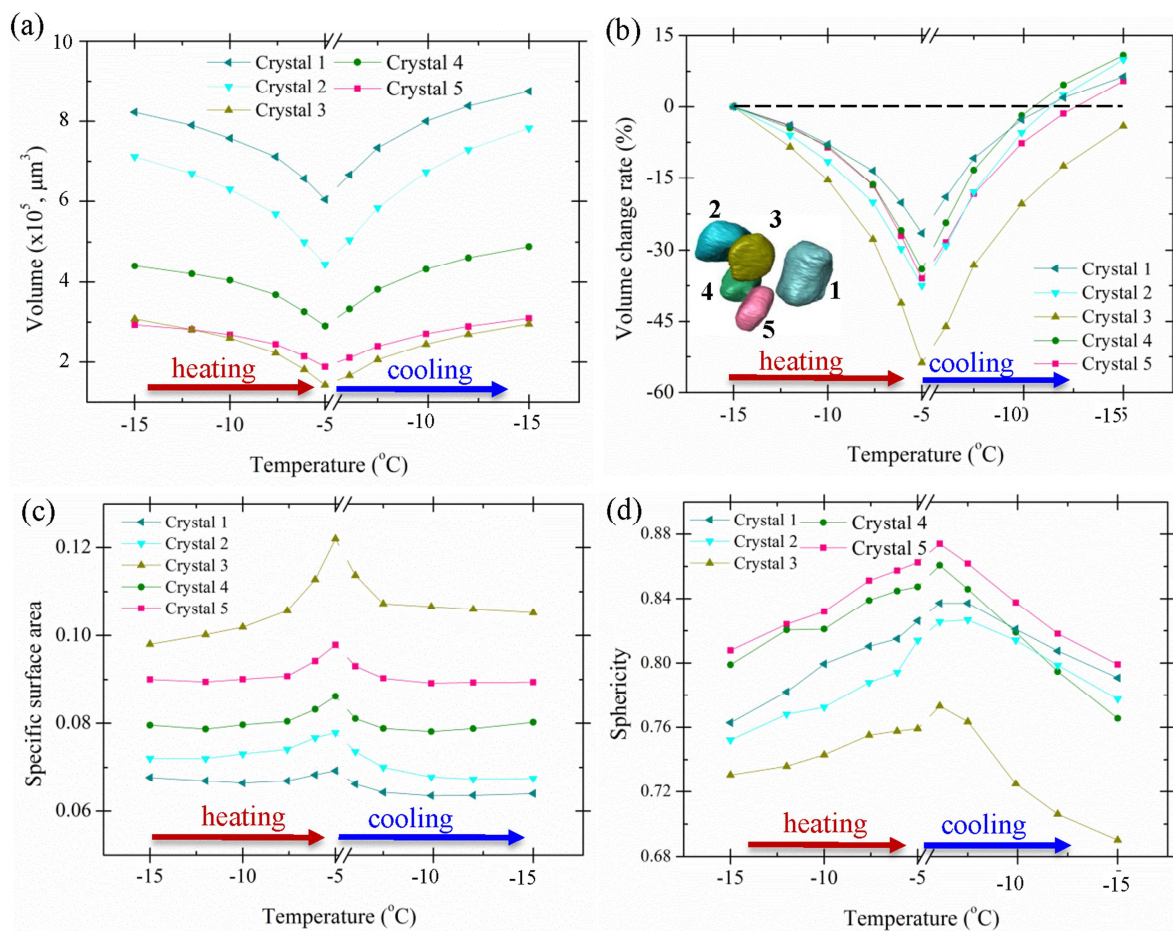


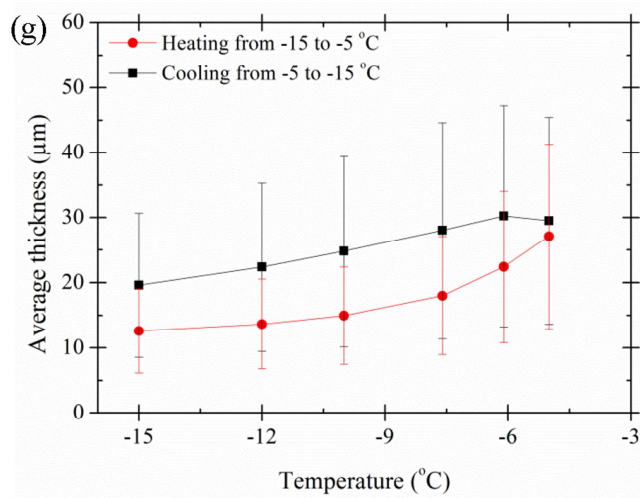
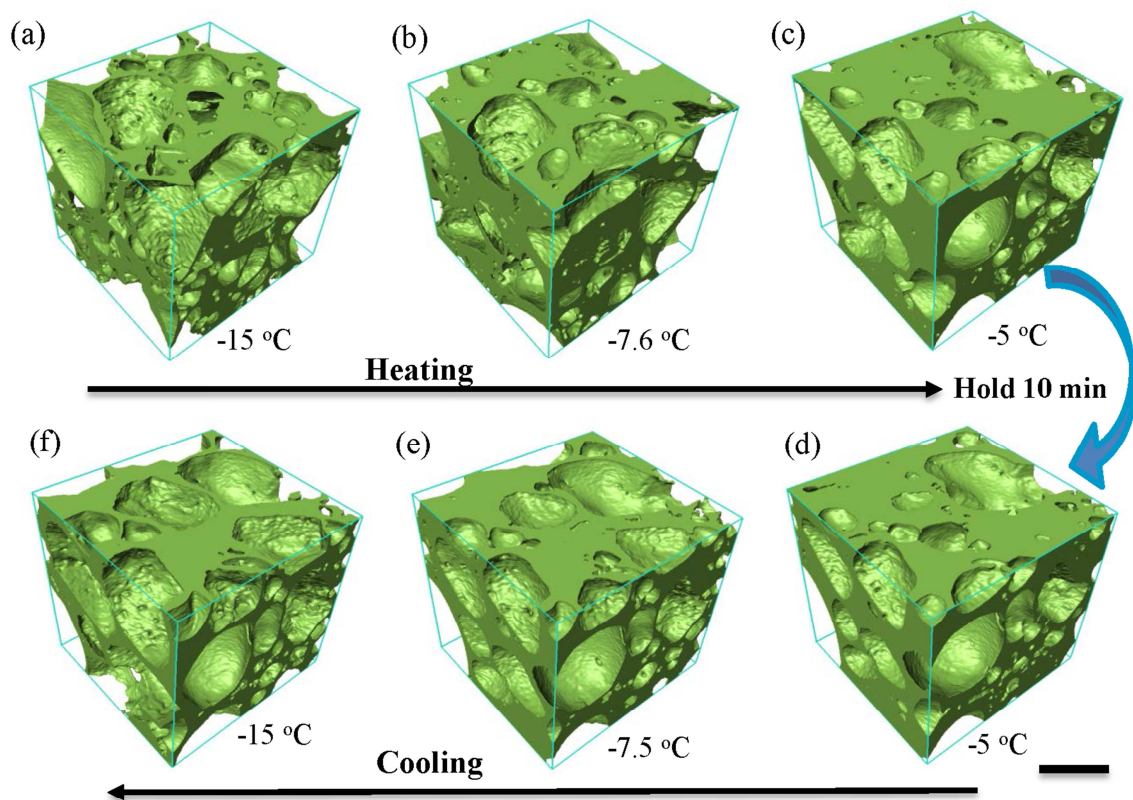


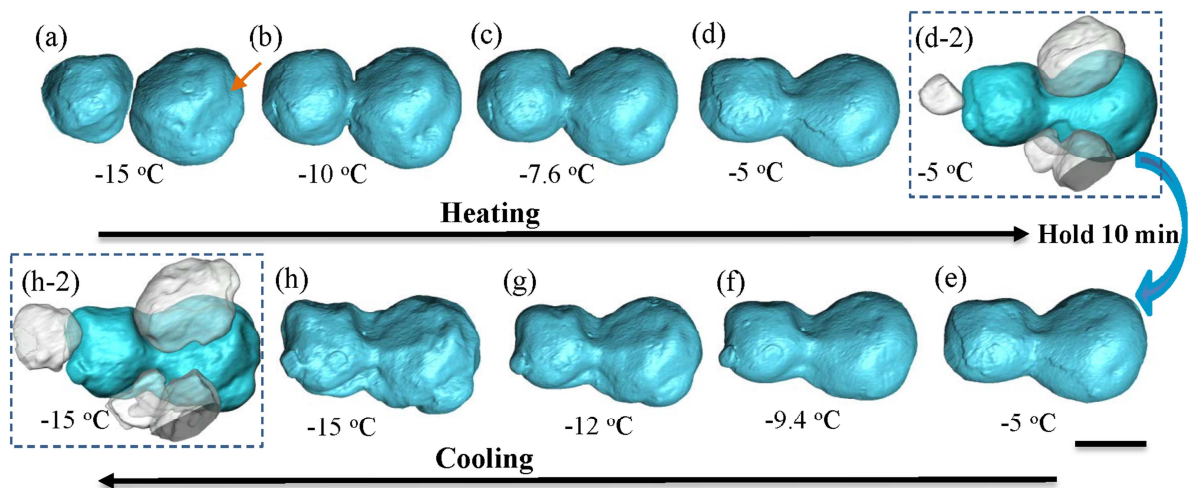


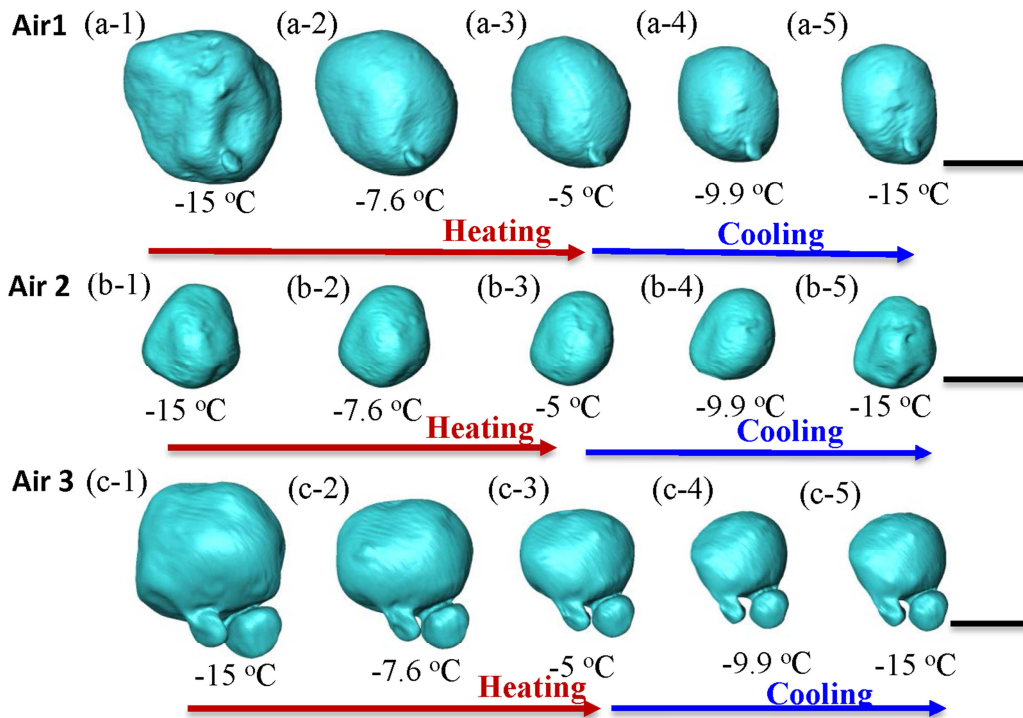


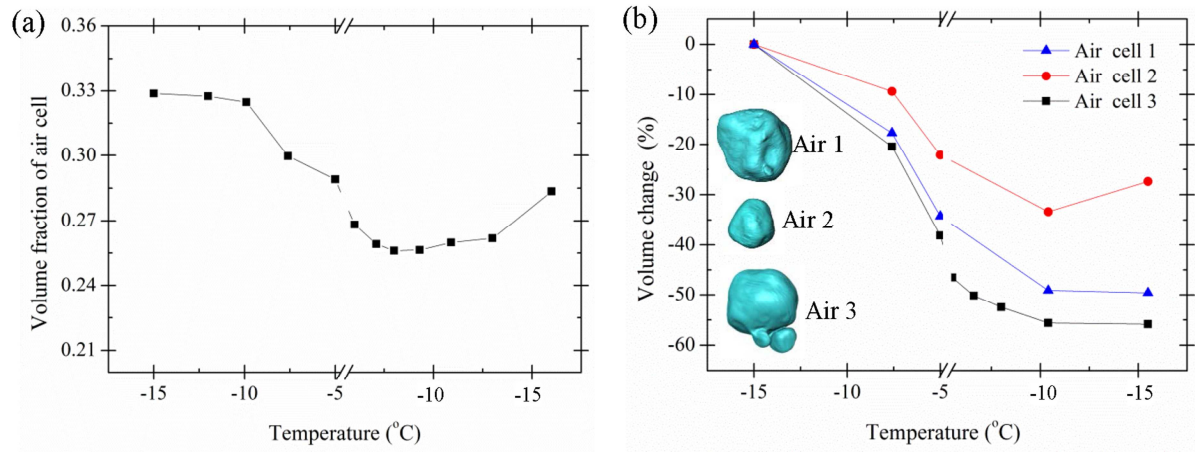












## Highlights

- In situ synchrotron tomography reveals the dynamics of ice cream emulsion's thermal stability
- A new tomographic data processing method was developed, enabling the features to be quantified
- The melting-recrystallization mechanism is responsible for ice crystal evolution
- Coalescence of air cells is the dominant coarsening mechanism controlling air bubble's evolution
- The unfrozen matrix is important in maintaining the ice cream's microstructural stability